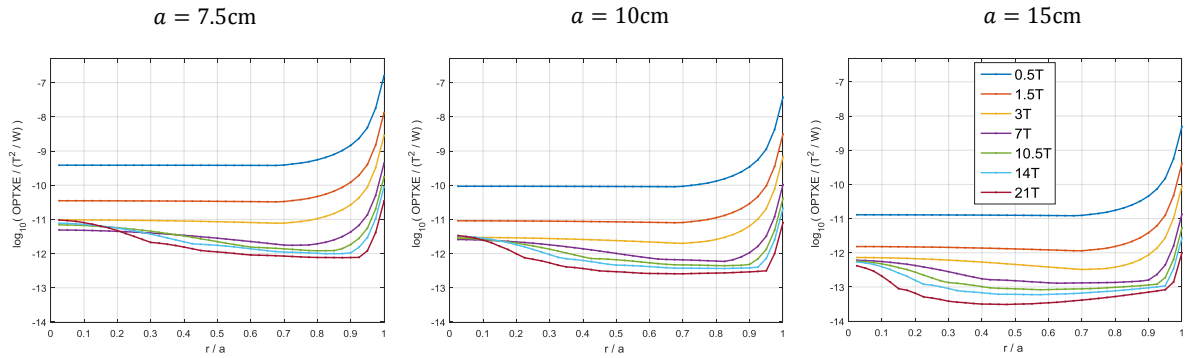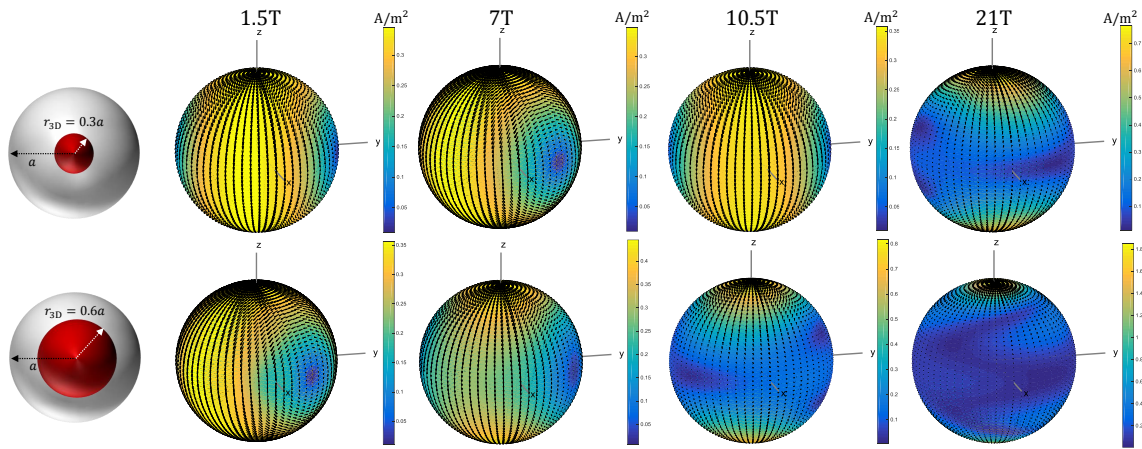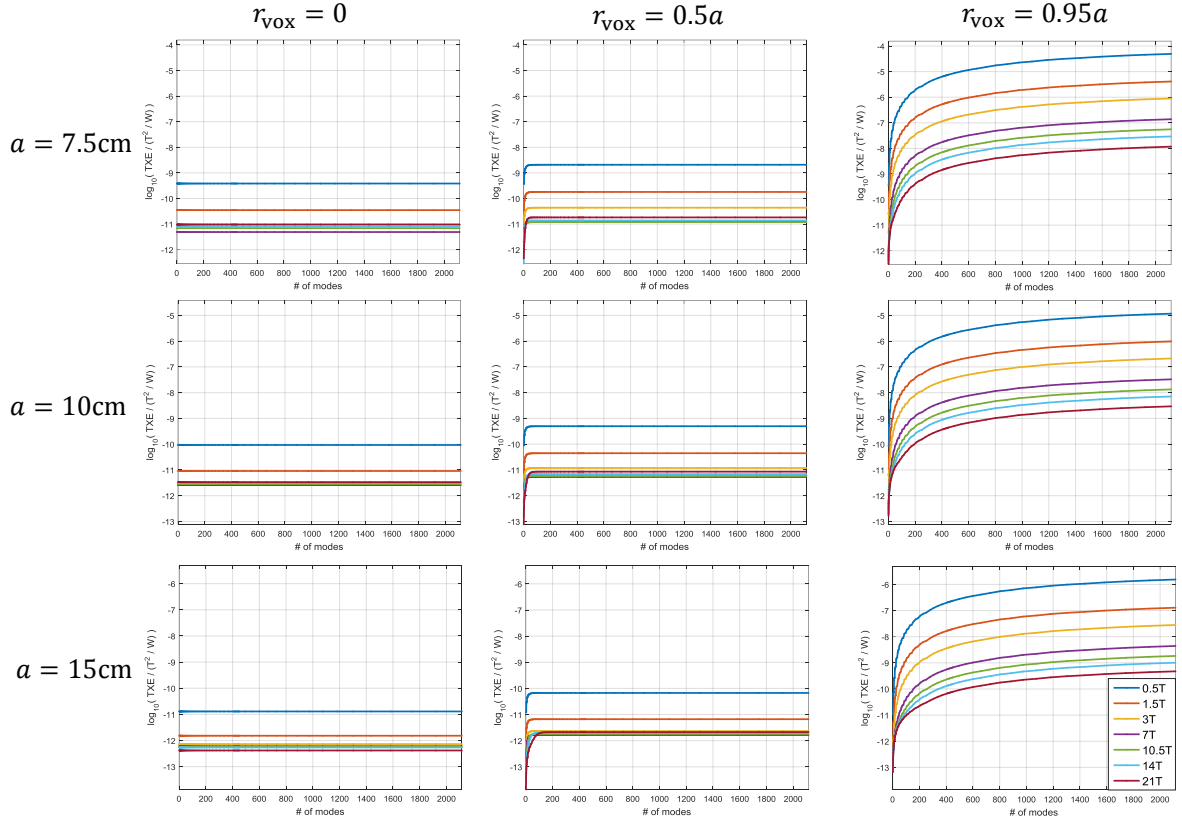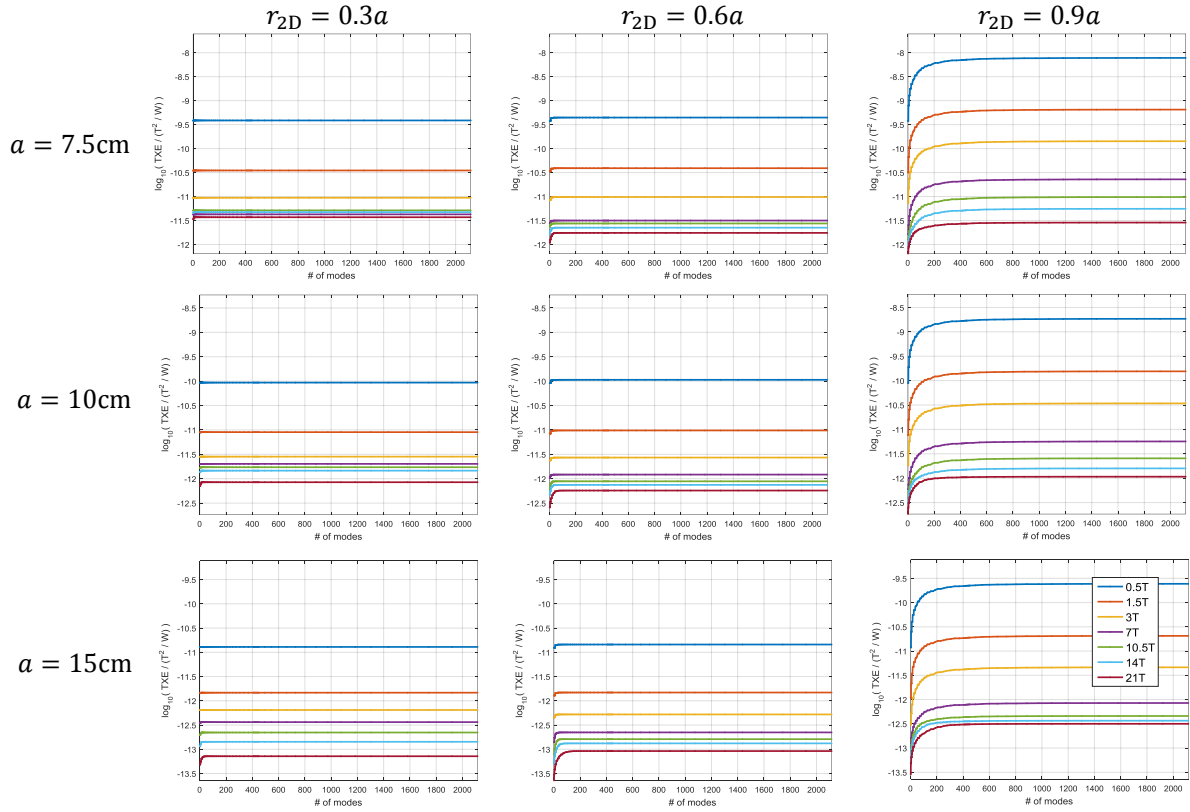# SUPPORTING INFORMATION

Supporting Information Figure S1: <mark>Optimal</mark> transmit efficiency as a function of the size of the three-dimensional excitation region of interest, for different spherical sample size and magnetic field strength. <mark>OPTXE</mark> is plotted in logarithmic scale for spherical samples with radii $a = 7.5, 10, 15$cm and brain-mimicking electrical properties, adjusted for each magnetic field strength. Similarly to the case of 2D ROI's (Figure 4), the <mark>OPTXE</mark> in 3D spherical ROI's remains approximately constant until the ROI approaches the size of the sphere, at which point it rapidly grows to its highest value.
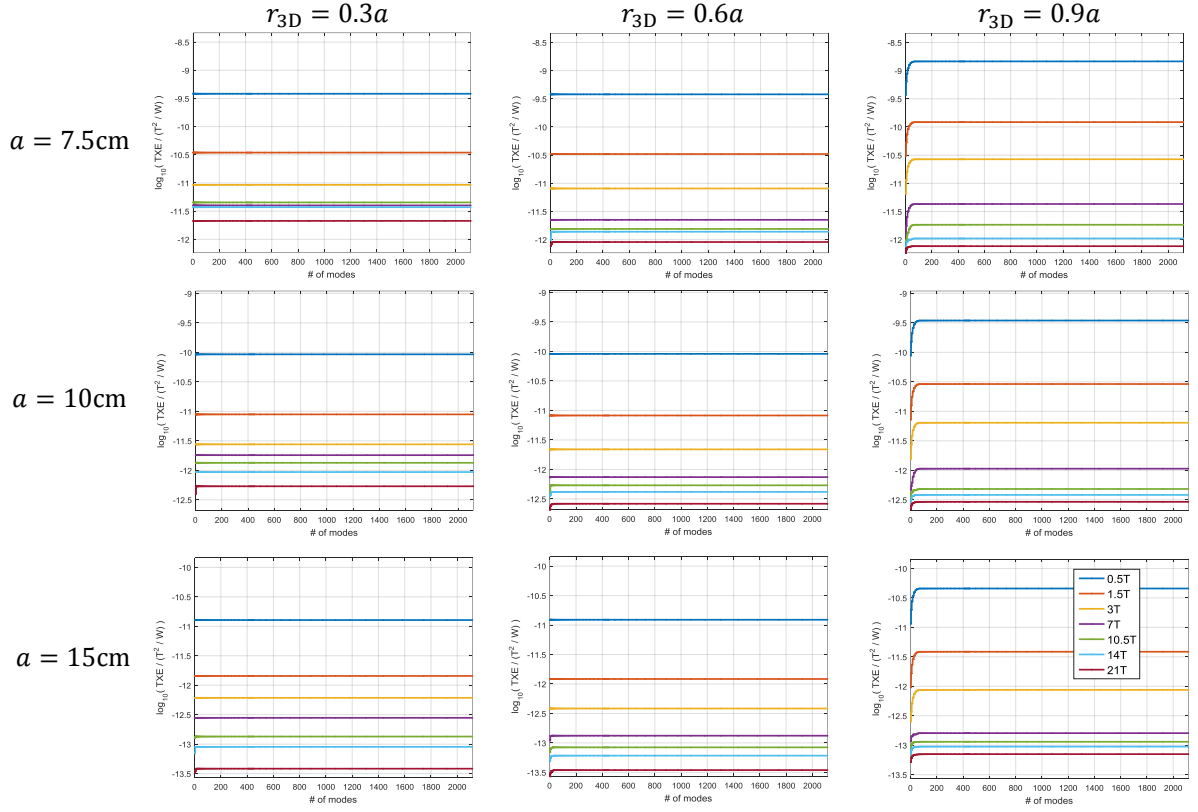

Supporting Information Figure S2: Snapshots of ideal current patterns yielding the <mark>optimal</mark> transmit efficiency, for two sizes of the three-dimensional excitation ROI and different main magnetic field strengths. The density of ideal current patterns at $\omega t = 0$ is shown for the spherical sample with radius $a = 10$cm, for the spherical 3D excitation ROI's of size $r_{3D} = 0.3a$ and $r_{3D} = 0.6a$, shown in the first column. Ideal current patterns are largely distributed around the sphere for $B_0 \leq 7$T, but they become more concentrated near the poles of the sphere at higher magnetic field strengths.
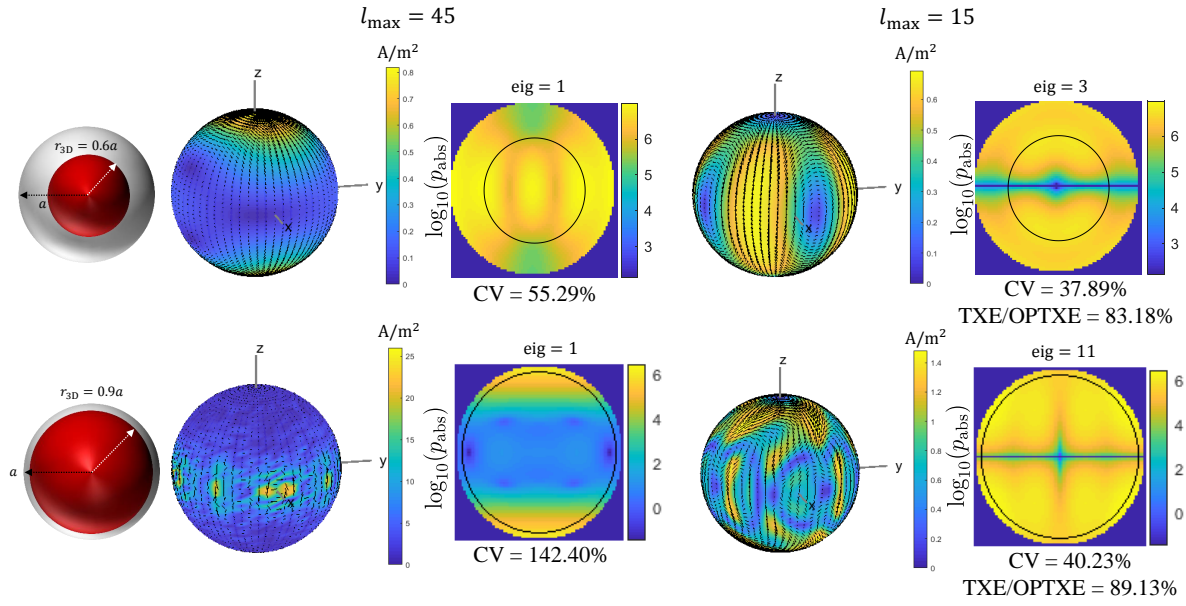
Supporting Information Figure S3: Convergence of the <mark>**optimal**</mark> **transmit efficiency calculations as a function of voxel location, for different main magnetic field strengths and object sizes.** <mark>OPTXE</mark> convergence is plotted in logarithmic scale for expansion order $l_{\max}$ ranging from 0 to 45, yielding a maximum of $N = (l_{\max} + 1)^2 = 2116$ modes. Note that each mode includes both the curl-free and divergence-free components in Equation 8. Results are shown for sphere radii $a = 7.5, 10, 15$cm and uniform brain-mimicking electrical properties adjusted for the corresponding frequency at $B_0 = 0.5, 1.5, 3, 7, 10.5, 14, 21$T. The convergence was assessed for three voxel locations at $r_{\mathrm{vox}} = 0, 0.5a, 0.95a$. The closer a voxel is to the surface of the sphere the larger the number of modes required for convergence. The convergence is also slower at higher field strengths, which is more evident for larger object sizes and the intermediate voxel location.
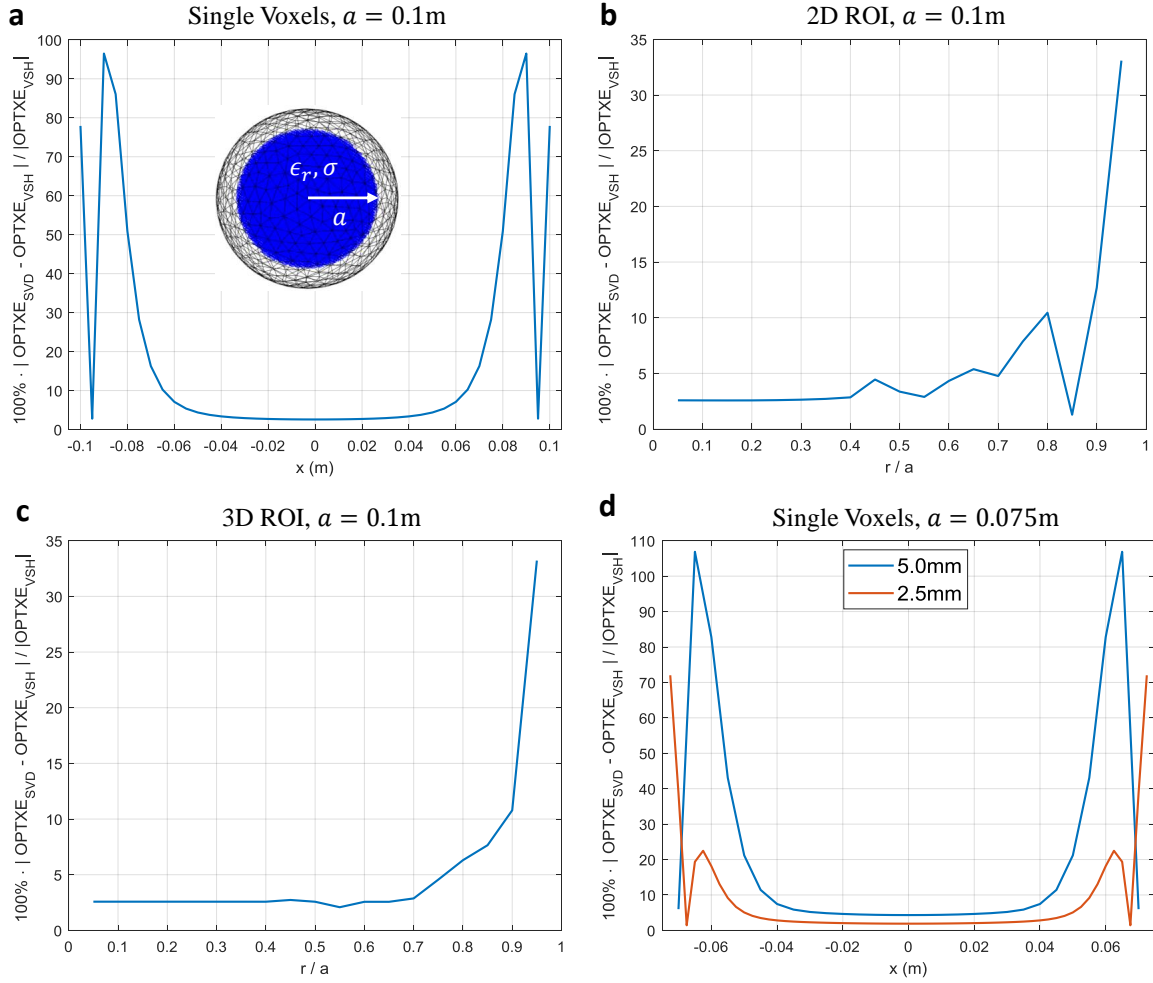
Supporting Information Figure S4: Convergence of the <mark>**optimal**</mark> **transmit efficiency calculations as a function of the size of the two-dimensional region of interest, for different main magnetic field strengths and object sizes.** <mark>OPTXE</mark> convergence is plotted for the same number of modes, sphere radii and B_0 shown in Supporting Information Figure S3, for different sizes $(r_{2D} = 0.3a, 0.6a, 0.9a)$ of a 2D circular disk ROI. More modes are required for convergence with larger excitation regions and at higher field strengths. This can be seen more clearly for larger object sizes and especially for the 2D ROI with $r_{2D} = 0.6a$.

Supporting Information Figure S5: Convergence of the <mark>optimal</mark> transmit efficiency calculations as a function of the size of the three-dimensional region of interest, for different main magnetic field strengths and object sizes. <mark>OPTXE</mark> convergence is plotted for different sizes $(r_{3D} = 0.3a, 0.6a, 0.9a)$ of a spherical 3D ROI concentric with the sample. Results are shown for the same range of expansion order, magnetic field strength and object size used in Supporting Information Figure S3. <mark>OPTXE</mark> for 3D ROI's converged faster than for the corresponding 2D ROI's. For example, for the large sphere $(a = 15\text{cm})$ and intermediate ROI size $(r_{3D} = 0.6a)$, the number of modes needed for convergence was 1, 5, 30 for 0.5T, 7T and 21T, respectively, which corresponds to 3%,11%,18% of the modes required for <mark>OPTXE</mark> convergence in 2D ROI's with the same radius (Supporting Information Figure S4).

Supporting Information Figure S6: Comparison between ideal current patterns yielding the optimal transmit efficiency and those more homogeneously distributed over the current-bearing surface to minimize B_1^+ inhomogeneity. While providing a theoretical optimum, ICP for large excitation ROI's could be difficult to realize in practice with existing multiple channel transmit technology. By limiting the expansion order of the electromagnetic basis used for the optimization ($l_{max} = 15$ vs. 45) and selecting the eigenvalue that maximizes B_1^+ homogeneity within the particular ROI, it is possible to obtain more realistic current patterns, while trading off only a small percentage of TXE. However, the resulting SAR could increase considerably.

Supporting Information Figure S7: Comparison between the proposed numerical framework and the analytic DGF framework for the calculation of OPTXE in a uniform sphere. OPTXE was calculated inside a 7.5 and a 10 cm radius uniform sphere ($\epsilon_r = 49.1$ and $\sigma = 0.61$S/m) at 7T. The current-bearing spherical shell was placed at 3 cm distance from the sphere. For the numerical case, the sphere was discretized with 5 mm resolution and the numerical basis was truncated with 10^{-5} approximation error. The relative error in the OPTXE with respect to the analytic solution remained small (around 2.5%) for voxels in the central region of the sphere, but increased for voxels closer to the edge, due to the staircase approximation of the curved surface of the sphere (a). The overall error was smaller for the case of OPTXE in 2D (b) and 3D (c) excitation ROI's. The error of the numerical calculation near the surface could drop significantly by refinement of the computational grid, as shown in (d). The resolution of the computational grid in the case of the head model was constrained to 5 mm by the memory size of the graphics processing unit.

Supporting Information Video S1: Animated version of Figure 3, showing ideal current patterns for single voxel excitations, precessing at the Larmor frequency for different values of the main magnetic field strength. Note that a PDF-viewer capable of Java-Script, such as the Adobe Acrobat Reader, is required in order to run the animation.

Supporting Information Video S2: Animated version of Figure 6, showing ideal current patterns for different sizes of the two-dimensional excitation region, precessing at the Larmor frequency for various magnetic field strengths. Note that a PDF-viewer capable of Java-Script, such as the Adobe Acrobat Reader, is required in order to run the animation.

Supporting Information Video S3: Animated version of Supporting Information Figure S2, showing ideal current patterns for different three-dimensional excitation regions, precessing at the Larmor frequency for various magnetic field strengths. Note that a PDF-viewer capable of Java-Script, such as the Adobe Acrobat Reader, is required in order to run the animation.